PNAS RESEARCH ARTICLE | EARTH, ATMOSPHERIC, AND PLANETARY SCIENCES OPEN ACCESS

Increased flood exposure in the Pacific Northwest following earthquake-driven subsidence and sea-level rise

Tina Dura[a,1], William Chilton[a,b], David Small[c], Andra J. Garner[d], Andrea Hawkes[e], Diego Melgar[c], Simon E. Engelhart[f], Lydia M. Staisch[g], Robert C. Witter[h], Alan R. Nelson[i], Harvey M. Kelsey[j], Jonathan C. Allan[k], David Bruce[a], Jessica DePaolis[a], Michael Priddy[a], Richard W. Briggs[i], Robert Weiss[a], SeanPaul La Selle[l], Michael Willis[a], and Benjamin P. Horton[m,n,o]

Affiliations are included on p. 8.

Edited by Michael Manga, University of California, Berkeley, CA; received December 2, 2024; accepted February 27, 2025

Climate-driven sea-level rise is increasing the frequency of coastal flooding worldwide, exacerbated locally by factors like land subsidence from groundwater and resource extraction. However, a process rarely considered in future sea-level rise scenarios is sudden (over minutes) land subsidence associated with great (>M8) earthquakes, which can exceed 1 m. Along the Washington, Oregon, and northern California coasts, the next great Cascadia subduction zone earthquake could cause up to 2 m of sudden coastal subsidence, dramatically raising sea level, expanding floodplains, and increasing the flood risk to local communities. Here, we quantify the potential expansion of the 1% floodplain (i.e., the area with an annual flood risk of 1%) under low (~0.5 m), medium (~1 m), and high (~2 m) earthquake-driven subsidence scenarios at 24 Cascadia estuaries. If a great earthquake occurred today, floodplains could expand by 90 km^2 (low), 160 km^2 (medium), or 300 km^2 (high subsidence), more than doubling the flooding exposure of residents, structures, and roads under the high subsidence scenario. By 2100, when climate-driven sea-level rise will compound the hazard, a great earthquake could expand floodplains by 170 km^2 (low), 240 km^2 (medium), or 370 km^2 (high subsidence), more than tripling the flooding exposure of residents, structures, and roads under the high subsidence scenario compared to the 2023 floodplain. Our findings can support decision-makers and coastal communities along the Cascadia subduction zone as they prepare for compound hazards from the earthquake cycle and climate-driven sea-level rise and provide critical insights for tectonically active coastlines globally.

earthquake hazards | coastal subsidence | sea-level rise | subduction zone hazards | compound hazards

Significance

In coastal flood hazard analysis, local factors like land subsidence from great earthquakes (>M8) are often overlooked. Along the Cascadia subduction zone (Washington to northern California), the next great earthquake will likely cause 0.5 to 2 m of sudden subsidence and associated sea-level rise, dramatically expanding coastal floodplains. Earthquake deformation modeling and geospatial analysis show that subsidence from a great earthquake at Cascadia today could double the flood exposure of residents, structures, and roads. By 2100, earthquake subsidence amplified by projected climate-driven sea-level rise could more than triple the flood exposure of residents, structures, and roads. This study underscores the need to consider combined earthquake and climate impacts in planning for coastal resilience at the Cascadia subduction zone and globally.

Climate-driven 21st-century sea-level rise is exposing coastal populations, infrastructure, and ecosystems around the world to more frequent marine inundation (1–4). At many coastal locations, downward vertical land motion (i.e., land subsidence) sometimes exceeding 5 mm/y is amplifying local relative sea-level rise (RSLR), defined as the change in sea level at a specific location relative to the land, and increasing flooding frequency (5–10). However, along much of the coast of Washington, Oregon, and northern California, gradual coastal uplift caused by crustal deformation during the interseismic phase of the current Cascadia subduction zone (CSZ) earthquake cycle locally mitigates the effects of climate-driven sea-level rise (11–14). Coastal uplift rates of 1 to 3 mm/y exceed the current rate of climate-driven sea-level rise at locations such as Astoria, OR, Port Orford, OR, and Crescent City, CA, with tide gauges recording RSL fall. At other locations, such as Yaquina Bay, OR, and Coos Bay, OR, where uplift rates are lower, tide gauges show 0.3 to 1.2 mm/y of RSLR, well below the global sea-level rise rate of 4.5 ± 1 mm/y (14–16). An exception is Humboldt Bay in Northern California, where complex regional tectonics are causing gradual subsidence, resulting in the highest recorded Pacific-coast RSLR rate of 4.7 mm/y (17).

The tectonic tempering of climate-driven sea-level rise along the Washington, Oregon, and northern California coasts is projected to be short-lived; by ~2030, rates of climate-driven sea-level rise are expected to outpace gradual uplift. By 2050, central (50th percentile) sea-level projections for a high emissions scenario [SSP3-7.0 (18) show 0.1 to 0.3 m of RSLR. By 2100, sea levels are projected to rise 0.4 to 0.9 m. The acceleration of RSLR will require Washington, Oregon, and northern California residents and planners to contend with compromised roadways and bridges, more frequently and/or permanently inundated lifelines and critical infrastructure, increased high-tide flooding and vulnerability to storm-surges, increased coastal erosion and barrier dune breaching, and eroding or inland-migrating coastal marshes (12, 19–21).

Author contributions: T.D., W.C., D.S., A.J.G., A.H., D.M., S.E.E., L.M.S., R.C.W., A.R.N., H.M.K., J.C.A., D.B., J.D., M.P., R.W.B., R.W., S.L., M.W., and B.P.H. designed research; T.D., W.C., D.S., and A.J.G. performed research; T.D., W.C., D.S., and A.J.G. analyzed data; and T.D., W.C., D.S., A.J.G., A.H., D.M., S.E.E., L.M.S., R.C.W., A.R.N., H.M.K., J.C.A., D.B., J.D., M.P., R.W.B., R.W., S.L., M.W., and B.P.H. wrote the paper.

The authors declare no competing interest.

This article is a PNAS Direct Submission.

[1]To whom correspondence may be addressed. Email: tinadura@vt.edu.

This article contains supporting information online at https://www.pnas.org/lookup/suppl/doi:10.1073/pnas.2424659122/-/DCSupplemental.

Published April 28, 2025.

Yet, gradual climate-driven sea-level rise is not the only inundation threat facing CSZ coastlines. Coastal subsidence from the next great (>M8) CSZ earthquake may produce >1 m of sudden RSLR much sooner than 2100 as evidenced in Cascadia's intertidal wetland stratigraphy (22, 23). Stratigraphic evidence of earthquake-driven subsidence from the most recent great earthquake along the CSZ, which occurred on 26 January 1700 CE, indicates sudden (over minutes) 0.5 to 2 m RSLR, resulting in submergence of low-lying intertidal wetlands and floodplains that may persist for decades to centuries after an earthquake (23–29). Radiocarbon dating of plant fragments preserved within pre-earthquake peat or overlying mud suggests >11 great earthquakes along Cascadia's coasts in the last 6 to 7 ka, recurring every ~200 to 800 y (30).

Earthquake-driven coastal subsidence following recent historical earthquakes has had severe consequences for communities, leading to permanent land loss, infrastructure damage, and forced relocation(31, 32). The 1960 Chile earthquake caused up to 2.5 m of coastal subsidence, permanently submerging coastal pine forests and farms and converting them to intertidal marshes (33), and flooding coastal towns and forcing residents to abandon homes and rebuild inland (34). In 1964, the Alaska earthquake lowered coastal areas by over 2 m, rendering roads, docks, and waterfront areas uninhabitable, in some cases necessitating relocation of communities to higher ground or raising waterfront facilities and airstrips above high tide (35). The 2004 Sumatra–Andaman earthquake caused land subsidence of up to a meter that led to chronic tidal flooding in waterfront areas used for aquaculture, resulting in oversalinization (36), and causing coastal erosion and land loss (36). Similarly, the 2011 Tōhoku earthquake in Japan caused up to 1 m of subsidence, disrupting ports (37), causing shoreline erosion (38), and permanently altering the morphology of river mouths (39).

At the CSZ, the National Seismic Hazard Model calculates a time-independent 15% probability of a M ≥ 8 rupture sometime in the next 50 y (40). Such an earthquake could suddenly lower coastal areas by 0.5 to 2 m, drastically altering shorelines and causing profound, lasting impacts to coastal populations, infrastructure, and ecosystems. Unlike gradual climate-driven RSLR, this earthquake-driven RSLR will happen within minutes, leaving no time for adaptation or mitigation. Moreover, climate-driven sea-level rise will make coastal areas even more vulnerable to the effects of future earthquake-driven subsidence as it progresses paired with the increased probability (29%) of a M ≥ 8 earthquake occurring by 2100 (40).

Here, we use earthquake rupture and deformation modeling in combination with geospatial analysis to quantify the projected expansion of coastal floodplains at 24 CSZ estuaries and surrounding communities if earthquake-driven subsidence occurs today (2023), or in 2100, when projected climate-driven RSLR will amplify flooding. We assess the impacts of expanded floodplains on land use, residents, structures, and roads, illustrating the importance of considering the compound hazards of earthquake- and climate-driven RSLR in coastal planning on the Pacific coast of the United States and other tectonically active coastlines.

Results

Effects of Earthquake-Driven Subsidence Today. Using 2023 as a baseline, we use geospatial analysis to quantify the expansion of the 1% floodplain area following earthquake-driven subsidence and its impact on land use, residents, structures, and roads (41–50) at 24 CSZ estuaries and surrounding communities (Fig. 1*A*; see the *Data Availability* section and *SI Appendix* for geospatial dataset information). The 1% (100-y) floodplain includes land that is covered in water during a flood that has a 1% chance of being equaled or exceeded each year. We define the perimeter of the 1% floodplain as the 1% annual exceedance probability water level as measured at a series of National Oceanic and Atmospheric Administration (NOAA) tide gauges along the Washington, Oregon, and northern California coasts (51) (*Materials and Methods*). Our 1% floodplain perimeters are broadly aligned with the Federal Emergency Management Administration (FEMA) high-risk flood zones within which residents and businesses are required to have flood insurance (52). To depict the floodplains, we overlayed the local 1% annual exceedance probability water-level boundary, which ranges from 1.08 to 1.23 m above mean higher high water (MHHW) (Fig. 1*C* and Table 1), on 10-m (1/3 arc-second) resolution digital elevation model (DEM) tiles (53) (*Materials and Methods*). We then adjusted the elevation of the 1% floodplain boundary upward by the modeled low (50th percentile), medium (10th percentile), and high (maximum recorded) earthquake-driven subsidence projections for each estuary defined in the FakeQuake Catalog, a forward modeling tool for earthquake ruptures used to simulate coseismic subsidence along the CSZ (54, 55) (Fig. 1 *B* and *C* and Table 1). These ruptures range in magnitude from 7.7 to 9.2 and were chosen due to their ability to match the coastal subsidence records correlated to the 1700 CE earthquake. The catalog includes fault slip heterogeneity and variable rupture areas, including both full-margin and smaller partial-margin ruptures. At the CSZ estuaries analyzed, the modeled low subsidence ranges from 0.23 to 0.67 m, the medium subsidence ranges from 0.46 to 1.34 m, and the high subsidence ranges from 0.93 to 2.67 m. For each subsidence scenario, we use a constant value of subsidence throughout the estuaries and limit our analysis to ~30 km inland from the coast due to the uncertainty in how coseismic subsidence will decay inland (56). Most sites analyzed lie within 10 km of the coastline, except for those in Washington, which extend out to our 30 km inland analysis limit. We note that we report the change in the floodplain area, rather than the total floodplain area before and after subsidence since some parts of the current 1% floodplain are already covered by water.

Our analysis shows that if a CSZ earthquake occurred today, earthquake-driven subsidence would increase the area of the 1% floodplain at the 24 estuaries by 90 km^2 (low subsidence), 160 km^2 (medium subsidence), or 300 km^2 (high subsidence; Table 2, Figs. 2 and 3 and *SI Appendix*, Figs. S1–S53). The land-use categories with the largest increase in land area within the 1% floodplain are parks and open space (340 km^2 to 410 km^2) and farm use (100 km^2 to 160 km^2) under the high subsidence scenario. Other notable impacts to land use under the high subsidence scenario include increased exposure to flooding of residential and rural residential (60 km^2 to 100 km^2) and commercial (100 km^2 to 120 km^2) land.

Along with impacts to land use, earthquake-driven subsidence will cause significant impacts to coastal residents, structures, and roads (Table 2, Fig. 2 and 3 and *SI Appendix*, Figs. S1–53). Within the 2023 1% floodplain at the 24 estuaries, there are 8,120 residents, 13,370 structures, and 700 km of roadway exposed to flooding. Following high-end earthquake-driven subsidence today, an additional 14,350 residents (177% increase), 22,500 structures (168% increase), and 1,250 km of roadway (179% increase) are estimated in the 1% floodplain, more than doubling flood exposure.

Postseismic land-level change occurring in the months to years after the next great CSZ earthquake could either temper or exacerbate coseismic subsidence. Luo et al. (2022) (58) modeled the

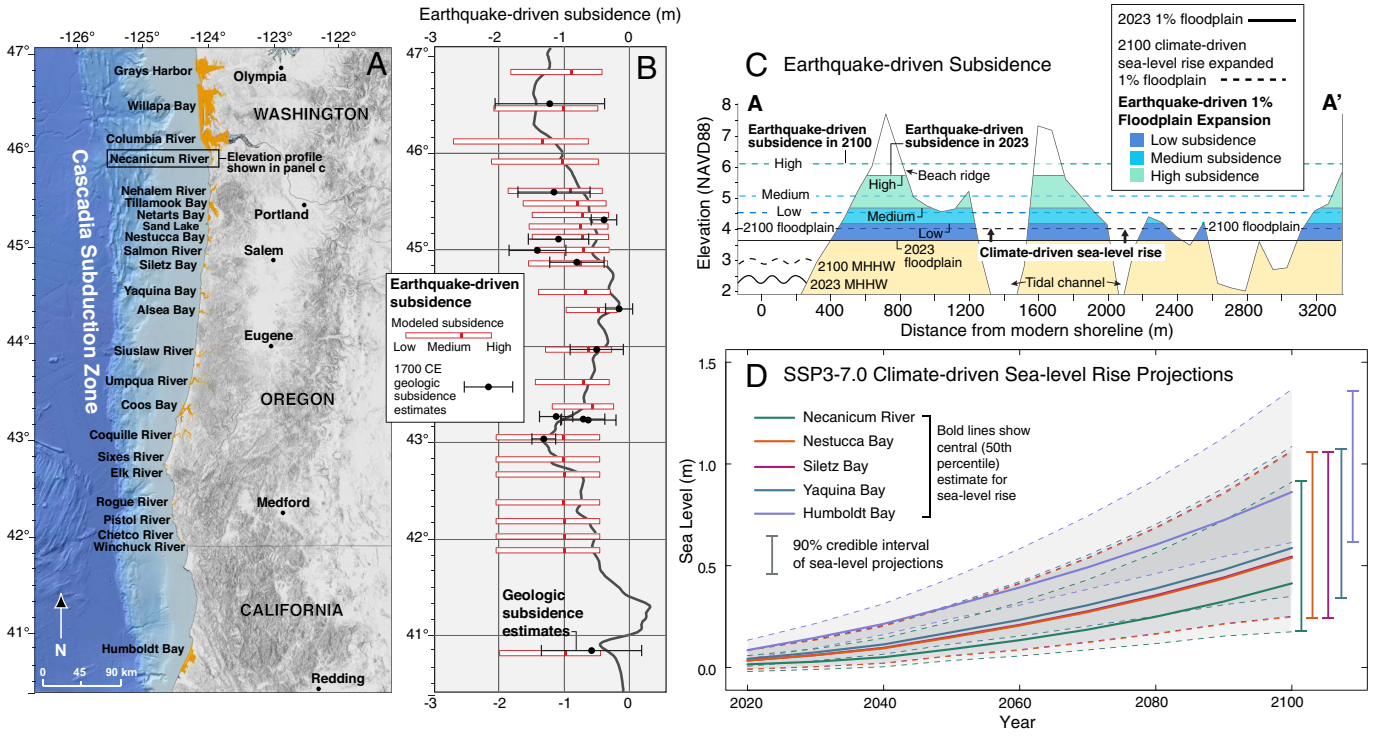

Fig. 1. (*A*) Washington, Oregon, and California coastal estuaries analyzed in this study. The orange polygons depict the 1% floodplain after high earthquake-driven subsidence in 2023 (defined baseline year). (*B*) Modeled earthquake-driven subsidence values (red rectangles) constrained by 1700 CE earthquake geologic subsidence estimates (black dots with uncertainties (23, 57) for each estuary). The dark gray continuous line shows one example of the medium subsidence from a full-margin rupture scenario from the FakeQuake Catalog (55). (*C*) Cross-section from the Necanicum River estuary showing current MHHW and 1% floodplain elevations and the shift upward that occurs following both earthquake-driven subsidence and climate-driven RSLR. Location of *A* and *A′* in map view is shown in Fig. 3*A*. (*D*) Climate-driven local sea-level rise projections based on the IPCC AR6 SSP3-7.0 (18) scenario for select sites spanning the CSZ. Upper and lower bounds of each curve are the 5th to 95th percentile range. In this study, we use the 50th percentile values. Projections for all sites are available in Table 1.

coseismic and postseismic deformation of the 1700 CE CSZ earthquake along coast-perpendicular profiles in southern Washington and northern Oregon and found that postseismic deformation from viscoelastic relaxation is negligible after 1 y, but afterslip—the slip that may occur between the Episodic Tremor and Slip zone and the seismogenic zone—could produce decimeters of uplift along the coast, depending on the downdip width of the afterslip. Also at the CSZ, high-resolution dating of post-1700 CE sediments shows the reestablishment of intertidal wetlands following coseismic subsidence takes centuries, suggesting a sustained submergence of the coast (29).

At other subduction zones, geodetic studies following the 2004 Mw 9.2 Sumatra–Andaman earthquake and the 2011 Mw 9.0 Tōhoku earthquake show that in some locations, coseismic subsidence has been exacerbated by continued postseismic subsidence (59–61), while other studies found that coastal locations recovered between 10%-50% of their subsidence through postseismic uplift within years (61, 62). At the CSZ, the magnitude and direction of postseismic deformation following a future great earthquake is uncertain. For the purposes of our study, postseismic land-level change may, for example, cause projected subsidence to increase from the "medium" to "high" scenario, or decrease from the medium to "low" scenario, depending on postseismic land-level change.

Amplified Impacts of Earthquake-Driven Subsidence Under Climate-Driven Sea-Level Rise. The probability of a CSZ earthquake increases with time, and with time, climate-driven sea-level rise is projected to expand CSZ floodplains, compounding the impacts of earthquake-driven subsidence when it does occur. To explore this amplification effect, we use a central estimate (50th percentile) from the Intergovernmental Panel on Climate Change (IPCC) AR6 SSP3-7.0 localized RSLR projections (63) (18) (Fig. 1*D*) to depict the climate-driven expansion of the 1% floodplain at the 24 CSZ estuaries for the year 2100 (Figs. 2 and 3). SSP3-7.0 assumes emissions and temperatures rise steadily and CO_2 emissions roughly double from current levels by 2100 (63).

The central estimates of RSLR for 2100 along the Washington, Oregon, and northern California coasts range from 0.4 to 0.9 m (Table 1). Our geospatial analysis shows that by 2100, climate-driven sea-level rise is projected to increase the land area within the 1% floodplain by 100 km^2. This expansion of the 1% floodplain would produce similar land-use impacts to the low earthquake-driven subsidence scenario described in the previous section (Table 2).

In addition to leaving CSZ shorelines more vulnerable to high-tide flooding and storm impacts (20), the expansion of the 1% floodplain due to climate-driven RSLR will amplify the effects of earthquake-driven subsidence. If a CSZ earthquake occurs in 2100, compared to the 2023 1% floodplain, combined climate-driven RSLR and earthquake-driven subsidence would increase the land area within the 1% floodplain by 170 km^2 (low subsidence), 240 km^2 (medium subsidence), or 370 km^2 (high subsidence; Table 2 and Figs. 2 and 3). The land-use categories with the largest increase in land area within the 1% floodplain continue to be parks and open space (340 km^2 to 430 km^2), farm use (100 km^2 to 180 km^2), residential and rural residential (60 km^2 to 120 km^2), and commercial (100 km^2 to 130 km^2) under the combined climate-driven SLR and high-subsidence scenario compared to the 2023 1% floodplain.

The combined effects of climate-driven RSLR and earthquake-driven subsidence amplify the impact to coastal residents, structures,

Table 1. *Low (50th percentile), medium (10th percentile), and high (maximum recorded) earthquake-driven subsidence values modeled with the FakeQuakes module (Small and Melgar, 2021)

Site	Earthquake-driven Subsidence*			Starting elevation of 1% floodplain, relative to MHHW** in meters	Climate-driven sea-level rise in 2100 in meters***
	Low (m)	Medium (m)	High (m)		
Grays Harbor	0.45	0.90	1.80	1.20	0.44
Willapa Bay	0.51	1.02	2.05	1.20	0.44
Columbia	0.67	1.34	2.67	1.20	0.41
Necanicum River	0.52	1.04	2.08	1.20	0.41
Nehalem Bay	0.46	0.91	1.83	1.21	0.54
Tillamook Bay	0.40	0.80	1.59	1.21	0.54
Netarts Bay	0.36	0.73	1.45	1.22	0.54
Sand Lake	0.37	0.75	1.50	1.22	0.54
Nestucca River	0.36	0.73	1.45	1.22	0.54
Salmon River	0.35	0.70	1.41	1.22	0.54
Siletz Bay	0.38	0.75	1.51	1.23	0.54
Yaquina Bay	0.34	0.67	1.35	1.23	0.59
Alsea Bay	0.23	0.46	0.93	1.22	0.59
Siuslaw River	0.31	0.62	1.25	1.19	0.54
Umpqua River	0.35	0.70	1.41	1.16	0.56
Coos Bay	0.28	0.57	1.14	1.14	0.52
Coquille River	0.50	1.01	2.01	1.13	0.52
Sixes River	0.50	1.01	2.01	1.12	0.51
Elk River	0.50	1.01	2.01	1.12	0.51
Rogue River	0.50	1.01	2.01	1.10	0.51
Pistol River	0.50	1.01	2.01	1.09	0.51
Chetco River	0.50	1.01	2.01	1.08	0.39
Winchuck River	0.50	1.01	2.01	1.08	0.39
Humboldt/Eureka	0.49	0.98	1.96	1.09	0.86

**MHHW. ***50th percentile value of the IPCC AR6 SSP3-7.0 local sea-level projections for each estuary in this study.

and primary roads (Table 2 and Figs. 2 and 3). Compared to the 2023 1% floodplain, high-end earthquake-driven subsidence amplified by climate-driven RSLR in 2100 more than triples flood exposure. This most extreme scenario would expose an additional 17,710 residents (218% increase), 29,060 structures (217% increase), and 1,620 km of roadway (231% increase) to flooding.

Discussion

The Cascadia Rising Scenario conducted in 2016 and 2022 outlined the potential impacts of shaking, tsunami inundation, landslides, and liquefaction from a ~M9 CSZ earthquake in Oregon and Washington, projecting >30,000 casualties, 2,000 destroyed bridges, >170,000 damaged or destroyed coastal structures, and heavy damage to >75% of coastal roadways, >60% of coastal fire stations, >75% of coastal schools, and >80% of seaports, for a resulting economic impact of >$81 billion (64–66). However, the potential effects of earthquake-driven subsidence, which may persist over decades to centuries, and the additional flooding exposure it will cause has not been previously quantified and could substantially increase the timeline to recovery.

Our results demonstrate the significant and lasting effects that sudden earthquake-driven subsidence would have on low-lying coastal communities along the CSZ and, therefore, the need for considering subsidence in future hazard assessments. We also highlight the role that 21st-century climate-driven RLSR will have in amplifying the impacts of a future earthquake. If a great CSZ earthquake occurred today, between 90 km^2 (low subsidence) and 300 km^2 (high subsidence) of low-lying coastal land area would be lowered into the 1% floodplain by earthquake-driven subsidence. The greatest impacts to people and infrastructure (i.e., structures and roads) are in the more densely populated areas of southern Washington, northern Oregon, and northern California. Farmlands developed for cattle grazing and farming through diking and draining in the early 20th century (42, 67) are one of the most heavily impacted land-use categories along the CSZ. More frequent marine inundation of farmlands will result in salination of agricultural soils and higher salt levels in groundwater, resulting in substantial economic losses (68, 69).

In Oregon, our 2023 high-earthquake-driven subsidence scenario depicts a similar amount of flooding as detailed in the Oregon Sea-Level Rise Inventory for Oregon's estuaries (20) in 2100, which shows that such an expansion of the 1% floodplain would impact 5 airports, 18 critical facilities (e.g., public schools, hospitals, fire stations, police stations, city halls, etc.), 8 wastewater treatment plants, 1 electric substation, and 57 potential contaminant sources (animal feeding operations, gas stations, solid waste facilities, chemical storage, liquid waste storage). If the next earthquake occurs in 2100 (after climate-driven RSLR has already begun to impact the coast) and RSLR rates exceed postseismic and/or interseismic uplift rates, low-lying areas along the CSZ may never recover. Today, and more so in 2100, the

Table 2. The change in the land area, residents, structures, and roads in the 1% floodplain today (2023) and in 2100, and the impact of low, medium, and high earthquake-driven subsidence at each time period

	Change in 1% floodplain area (km^2)	Permanent residents in 1% floodplain	Total change	% change	Structures in 1% floodplain	Total change	% change	Kilometers of primary roadway in 1% floodplain	Total change	% change
2023 1% Floodplain		8120			13,370			700		
Low subsidence	90	11,100	2,980	37	18,180	4,810	36	990	290	41
Medium subsidence	160	14,740	6,620	82	23,830	10,460	78	1,300	600	86
High subsidence	300	22,470	14,350	177	35,870	22,500	168	1,950	1,250	179
2100 1% Floodplain	100	11,530	3,410	42	18,970	5,600	42	1,040	340	49
Low subsidence	170	15,000	6,880	85	24,550	11,180	84	1,350	650	93
Medium subsidence	240	19,060	10,940	135	30,350	16,980	127	1,670	970	139
High subsidence	370	25,830	17,710	218	42,430	29,060	217	2,320	1,620	231

Total change calculations are made relative to the starting 2023 value in each category. All values are rounded to the nearest 10.

immediate effect of earthquake-driven subsidence will be a delay in response and recovery to the earthquake due to compromised assets; long-term effects could render many coastal communities uninhabitable (70). Although we do not quantify damage to seaports, previous reports suggest that earthquake-driven subsidence will also compromise jetties, inlets, and navigation channels, affecting port operations and disaster response (65). Additionally, liquefaction and lateral spreading could locally amplify subsidence in river valleys, waterfronts, and artificially filled coastal locations where critical assets along the CSZ coastline are often located (66, 71).

Beyond the direct impacts on infrastructure, sudden earthquake-driven subsidence can appreciably impact natural systems—particularly coastal estuaries, intertidal wetlands, and protective dunes and beaches. Wetland loss is a concern: Intertidal wetlands typically migrate inland in response to rising sea levels, but this inland movement can be constrained by topography and human development. This is especially true along the Oregon

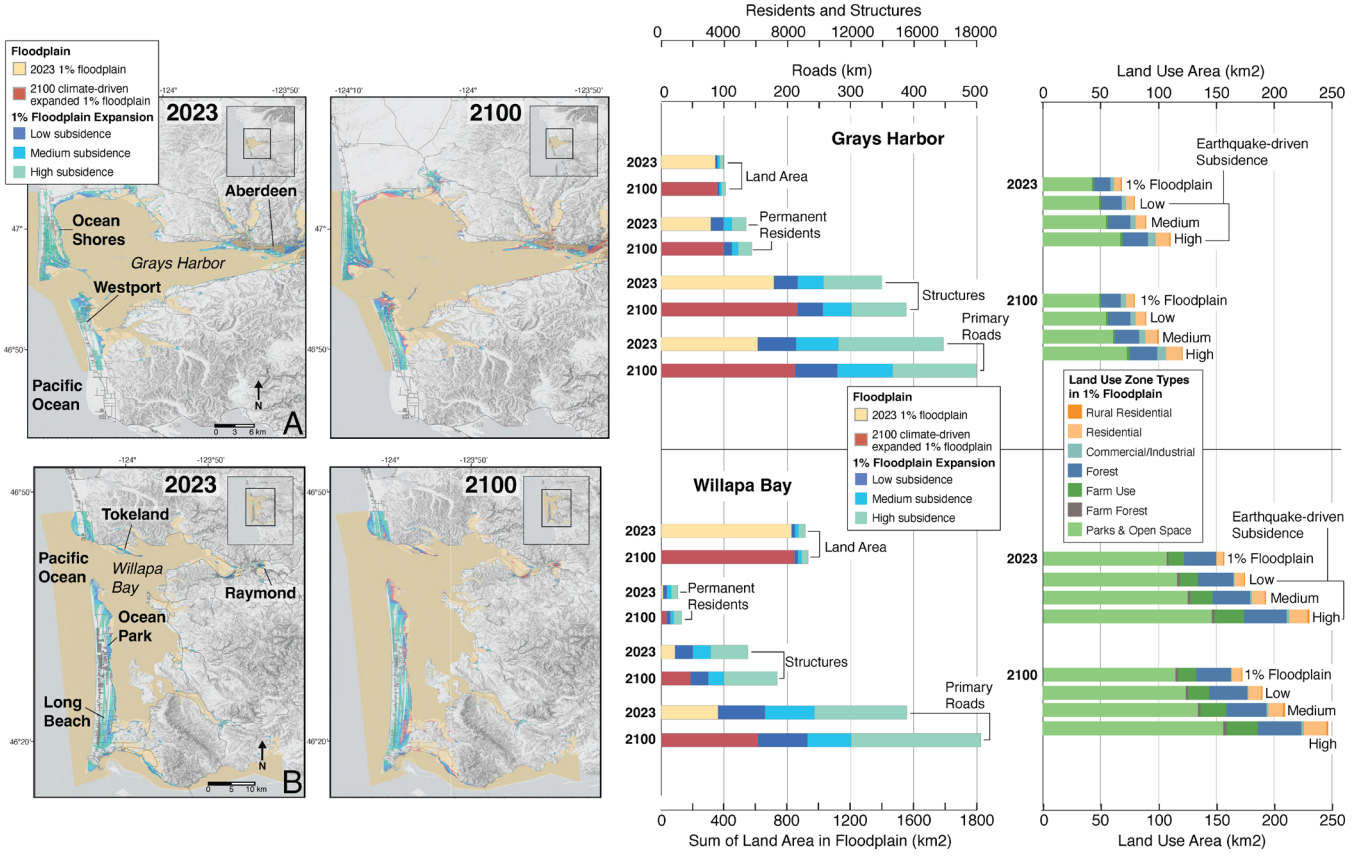

Fig. 2. Floodplain maps and bar graphs depicting the expansion of the 1% floodplain after earthquake-driven subsidence today (2023) and in 2100 when the earthquake-driven subsidence is amplified by climate-driven sea-level rise for (*A*) Grays Harbor, WA; and (*B*) Willapa Bay, WA. Bar graphs to the right of each map set show the amount of land area, number of residents, structures, roads, and different land-use types in the 1% floodplain following earthquake-driven subsidence today (2023) and in 2100, when the effects of earthquake-driven subsidence are amplified by climate-driven sea-level rise.

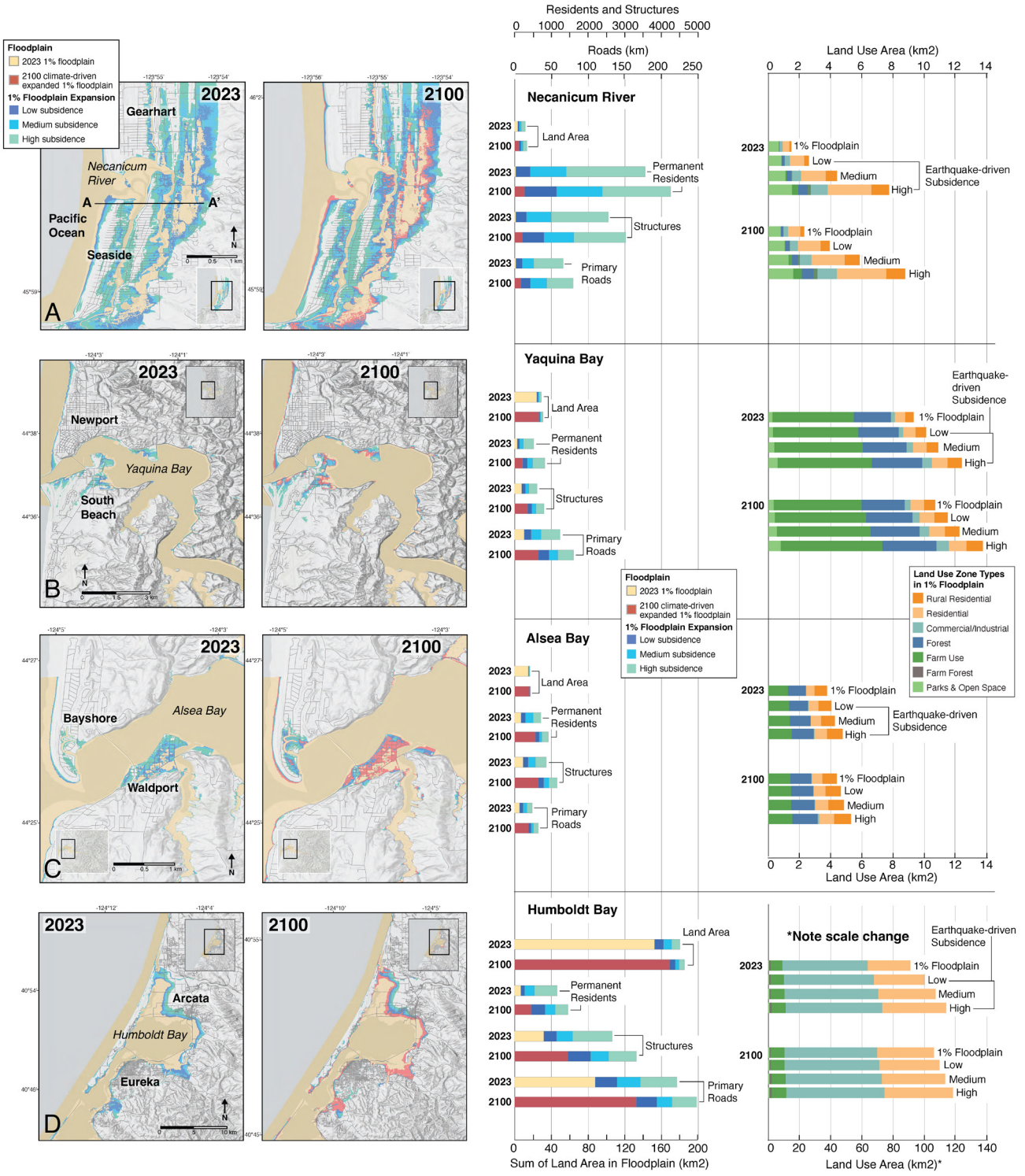

Fig. 3. Floodplain maps and bar graphs depicting the expansion of the 1% floodplain after earthquake-driven subsidence today (2023) and in 2100 when the earthquake-driven subsidence is amplified by climate-driven sea-level rise for the (*A*) Necanicum River, OR; (*B*) Yaquina Bay, OR; (*C*) Alsea Bay, OR; and (*D*) Humboldt Bay, CA. Bar graphs to the *Right* of each map set show the amount of land area, number of residents, structures, roads, and different land-use types in the 1% floodplain following earthquake-driven subsidence today (2023) and in 2100, when the effects of earthquake-driven subsidence are amplified by climate-driven sea-level rise.

coast, where Brophy et al. (2018) (21) demonstrated that a sea-level rise of ~2.7 m could lower ~50% of existing Oregon intertidal wetlands to mudflat elevations, a result comparable to that in this study's high-subsidence scenarios in 2100. Thorne et al. (2018) (72), who also considered intertidal wetland accretion rates, found that under ~1.4 m of RSLR, Oregon would lose all of its high and middle intertidal wetland environments. The loss of intertidal wetlands directly impacts ecosystem services such as water filtration, habitat for fisheries and shorebirds, and carbon storage capacity (72). Intertidal wetlands function as natural carbon sinks, and their erosion or conversion to tidal flats reduces their ability to sequester carbon (73). The erosion and drowning of coastal wetlands caused by earthquake-driven subsidence will also diminish their role as natural buffers against storm surges.

Intertidal wetlands can dissipate wave energy, keeping storm surges from penetrating inland and preventing sediment erosion and property damage (74, 75).

Earthquake-driven subsidence also puts ocean-exposed sandy coastlines at risk. For example, during the 2015 to 2016 El Niño year, a modest RSLR of 7 to 17 cm along the Pacific coast of the United States resulted in substantial coastal erosion, with shoreline retreat 70% greater than during normal winter conditions (76). Sudden earthquake-driven subsidence can also increase the tidal range within an estuary, exacerbating issues such as high-tide flooding and the impacts of storm surges coinciding with high tides. A study in the Columbia River estuary showed that projected earthquake-driven subsidence could result in up to a 10% increase in the local tidal range (22).

Finally, sudden earthquake-driven subsidence and climate-driven sea-level rise also need to be considered in tsunami inundation maps. The current tsunami inundation maps for Washington, Oregon, and California take into account the subsidence that will occur during the next CSZ earthquake and how this will increase tsunami inundation (77–79). However, tsunami hazard maps do not consider climate-driven sea-level rise and the amplification effect it will have on future tsunamis. (80) showed that under future climate-driven sea-level rise scenarios, tsunamis created by more common, smaller magnitude earthquakes can have the same coastal wave heights as rare, great-earthquake generated tsunamis. This lesser-considered effect of climate-driven RLSR, especially combined with earthquake-driven subsidence and tides, may imply increased flooding risk in future hazard assessments (80, 81).

Our findings stress the importance of incorporating the effects of earthquake-driven subsidence into future flood hazard assessments at the CSZ, as well as considering how climate-driven RLSR will amplify the impacts of a future earthquake and tsunami. Preparing for these compound hazards can minimize long-term damage, ensure resilient communities, and protect critical coastal ecosystems from permanent degradation. Given the global prevalence of subduction zones, these insights hold relevance beyond the CSZ, informing hazard assessments and mitigation strategies for tectonically active regions worldwide.

Materials and Methods

Geospatial Analysis. To assess the impacts of potential earthquake-driven and climate-driven sea-level rise, we created a series of "bathtub" style 1% floodplain contour polygons on 10-m (1/3 arc-second) resolution DEM tiles from the U.S. Geological Survey (USGS) National Map 3DEP data collection (53). The contour polygon elevations were determined from combinations of potential earthquake-driven subsidence and sea-level rise values. Site-specific 1% exceedance water level elevations are from the NOAA Tides and Currents database for sites at Astoria, OR, Charleston, OR, and South Beach, OR (51). For each site, we apply the closest 1% exceedance water level value to define the perimeter of the 1% floodplain. The starting elevation of the 1% floodplain at each site is reported in Table 1 relative to MHHW. The 1% floodplain contours presented here closely correspond to the FEMA "still water" elevations (82), and likely represent the lower end of potential impacts, as additional impacts from river flow, snow melt cycles, precipitation, and wave action are not included.

To quantify earthquake-driven subsidence and sea-level rise impacts, contour polygons were intersected with a variety of data including state and county-level land use zoning, road, structure footprint, and population data (41–50) (Dataset S1). To remove inconsistencies with land use data coding between states, a unified land use code was created for use in this study. Since a wide variety of subcategories existed within certain land zones like commercial and industrial, these subcategories were combined into a single category for the entire study area, eliminating regional coding discrepancies. We note that our starting 1% floodplain areas include open water and estuary land. Because of this, in the main text, we emphasize the change in land area in the 1% floodplain rather than the total area. For our land-use impacts analysis, we removed "shorelands" and "estuary" in order to focus more on on-land impacts. Despite open water sometimes being classified as "parks and open space", we kept it in the dataset because the "parks and open space" category is also often found on land.

Sea-Level Rise Projections. The IPCC AR6 sea-level change projections used in this work are medium-confidence projections for the SSP3-7.0 emissions scenario (83). The medium-confidence projections use methods and assumptions about the individual processes that contribute to sea-level change that are assessed to have medium confidence or stronger by the IPCC and therefore do not include contributions that could lead to more extreme sea-level rise, but which have lower confidence levels (such as Marine Ice Cliff Instability). The sea-level rise projections are provided on both a 1×1 degree grid, and at 1,030 tide gauge locations from around the world. The sea-level rise projections are provided in decadal time steps starting in 2020 and extending to the year 2150; here, we focus on the 50th percentile of projections for the year 2100 (18, 63)–and therefore do not account for the possibility of more extreme, tail-area sea-level rise totals.

For this work, we use the publicly available NASA Sea Level Projection tool (83) to isolate the projected sea-level rise at points that are most relevant for our work. This allows us to select the best sea-level rise value for each location on a case-by-case basis, whether that value comes from the nearest 1×1 degree ocean grid cell in the gridded sea-level rise dataset or a tide gauge location along the Pacific coast. Because sea-level rise values from the gridded dataset will have interpolations that capture vertical land motion to varying degrees of success, this manual approach to selecting sea-level rise projection values allows us to ensure that we are using the best sea-level projection for each site, based on how well vertical land motion is captured within both the gridded data and the tide gauge dataset.

Modeled and Observed Earthquake Subsidence Estimates. Subsidence estimates are calculated at each site based on about 1,600 kinematic, stochastic slip rupture models (54) of varying magnitudes between 7.7 and 9.2. These models come from a larger catalog of 37,500 hypothetical ruptures (55). Each of these ruptures is unique from one another, with rupture area, amount of slip, and location of dominant slip patches varying between ruptures. These ruptures were initially chosen based on their abilities to match the coastal subsidence records correlated to the 1700 CE event (23, 57). Subsidence estimates for the 1700 CE event are distributed along the entire length of the CSZ, likely representing a full-margin rupture. To account for the possibility of shorter or segmented rupture scenarios, each kinematic rupture model must reproduce the observed 1700 CE subsidence for sites located within 50 km of the modeled rupture area. This allows for a wider range of subsidence estimates to be modeled.

For each kinematic rupture model, coseismic subsidence is calculated at each site using the analytical solution for angular dislocations for triangular subfaults in an elastic half space (84). Based on 1,600 model results, three coseismic subsidence values are determined for each site: a small, medium, and high value. We base the high subsidence value on the largest subsidence modeled at each location to function as the "worst-case scenario." Stated prior, modeled subsidence values are validated with respect to coastal subsidence estimates previously determined for the 1700 CE event, although not all geologic sites with subsidence estimates are colocated with the 24 sites modeled in this study. As a result, modeled sites closest to the geologic sites with estimated subsidence values more closely resemble the upper bounds of the 1700 CE geologic subsidence estimates. Locations that are farther from sites with observed subsidence estimates are less constrained by the 1700 CE data, and as a result the models produced higher "worst-case scenario" subsidence estimates there (e.g., Sixes River, Elk River, Rogue River, Pistol River, Chetco River, Winchuck River, Oregon). Due to modeled subsidence estimates being unrealistically high at these locations, we used the closest, better constrained subsidence estimate (e.g., Coquille River) for these sites (Table 1). At the 24 sites, mean subsidence values are −0.4 m, −0.9 m, and −1.7 m for the low, medium, and high modeled subsidence values, respectively. The modeled subsidence values follow the low (50th percentile), medium (10th percentile), and high (maximum recorded) earthquake-driven subsidence values of the 1,600 ruptures for each site location.

Data, Materials, and Software Availability. All data integral to the stated conclusions are presented within the results, *Materials and Methods*, or *SI Appendix*. All shapefiles generated in this study are available at

https://github.com/DuraGEOSVT/Cascadia (85). Digital elevation models are publicly available at the following links: https://www.usgs.gov/the-national-map-data-delivery (53) and https://www.usgs.gov/3d-elevation-program. Geospatial analysis datasets are publicly available at the following links: https://geohub.oregon.gov/datasets/oregon-geo::zoning/about (86) (Oregon Land Use and Land Cover), https://humboldtgov.org/276/GIS-Data-Download (87) (California Land Use and Land Cover), https://geo.wa.gov/datasets/wa-geoservices::washington-state-land-use-2010/about (88) (Washington Land Use and Land Cover), https://www.arcgis.com/home/item.html?id=3bc7b-d2ef9e54f66886f4c095a6eb63c (89) (Oregon Roads), https://humboldtgov.org/276/GIS-Data-Download (90) (California Roads), https://www.co.pacific.wa.us/gis/DesktopGIS/WEB/index.html (91) (Pacific County Roads), https://www.graysharbor.us/departments/central_services/GISDataDownload.php (92) (Grays Harbor Roads), https://data.humdata.org/dataset/united-states-high-resolution-population-density-maps-demographic-estimates (93), https://fema.maps.arcgis.com/home/item.html?id=0ec8512ad21e4bb-987d7e848d14e7e24 - overview (94), and https://github.com/microsoft/USBuildingFootprints?tab=readme-ov-file (95) (all site structures).

ACKNOWLEDGMENTS. This work was supported by funding from NSF award to T.D. (EAR-1624795), T.D. and A.D.H. (EAR-2225286), and A.D.H. (EAR-1419846, OCE-2325311). B.P.H. is also supported by the Singapore Ministry of Education Academic Research Fund MOE2019-T3-1-004, the National Research Foundation Singapore, and the Singapore Ministry of Education, under the Research Centers of Excellence initiative. R.C.W., R.W.B., S.L., and A.R.N. are supported by the Earthquake Hazard Program of the U.S. Geological Survey. H.M.K. is supported by the external grants program of the USGS National Earthquake Hazards Reduction Program. This work is a contribution to PALSEA-Next (Palaeo-Constraints on Sea-Level Rise) and the International Geoscience Programme Project 725. This work is Earth Observatory of Singapore contribution 646. This research was supported in part by an appointment to the Department of Defense (DOD) Research Program administered by the Oak Ridge Institute for Science and Education (ORISE) through an interagency agreement between the U.S. Department of Energy (DOE) and the DOD. ORISE is managed by Oak Ridge Associated Universities (ORAU) under DOE contract number SC0014664. All opinions expressed in this paper are the author's and do not necessarily reflect the policies and views of DOD, DOE, or ORAU/ORISE. Any use of trade, firm, or product names is for descriptive purposes only and does not imply endorsement by the U.S. Government. We thank the sea-level rise projection authors for developing and making the sea-level rise projections available, multiple funding agencies for supporting the development of the projections, and the NASA Sea-Level Change Team for developing and hosting the Intergovernmental Panel on Climate Change Sixth Assessment Report Sea-Level Projection Tool.

Author affiliations: [a]Department of Geosciences, Virginia Tech, Blacksburg, VA 24061; [b]Water Resources, Singhofen Halff Associates, Orlando, FL 32817; [c]Department of Earth Sciences, University of Oregon, Eugene, OR 97403; [d]Department of Environmental Science, Rowan University, Glassboro, NJ 08028; [e]Department of Earth and Ocean Sciences, University of North Carolina, Wilmington, NC 28403; [f]Department of Geography, Durham University, Durham DH1 3LE, United Kingdom; [g]Geology, Minerals, Energy, and Geophysics Science Center, U.S. Geological Survey, Portland, OR 97201; [h]Alaska Science Center, U.S. Geological Survey, Anchorage, AK 99508; [i]Earthquake Hazards Program, U.S. Geological Survey, Golden, CO 80401; [j]Department of Geology, California State Polytechnic University, Humboldt, Arcata, CA 95521; [k]Department of Geology and Mineral Industries, Geohazards, Newport, OR 97365; [l]Pacific Coastal and Marine Science Center, U.S. Geological Survey Santa Cruz, CA 95060; [m]School of Energy and Environment City University of Hong Kong, Hong Kong, China; [n]Earth Observatory of Singapore, Nanyang Technological University, Singapore, Singapore 639798; and [o]Asian School of the Environment, Nanyang Technological University, Singapore, Singapore 639798

1. M. E. Hauer, J. M. Evans, D. R. Mishra, Millions projected to be at risk from sea-level rise in the continental United States. *Nat. Clim. Change* **6**, 691–695 (2016).
2. S. Vitousek *et al.*, Doubling of coastal flooding frequency within decades due to sea-level rise. *Sci. Rep.* **7**, 1399 (2017).
3. R. S. Nerem *et al.*, Climate-change–driven accelerated sea-level rise detected in the altimeter era. *Proc. Natl. Acad. Sci. U.S.A.* **115**, 2022–2025 (2018).
4. V. Masson-Delmotte *et al.*, Climate change 2021: The physical science basis. *Contrib. Work. Group Sixth Assess. Rep. Intergov. Panel Clim. Change* **2**, 2391 (2021).
5. C. Tay *et al.*, Sea-level rise from land subsidence in major coastal cities. *Nat. Sustain.* **5**, 1049–1057 (2022).
6. M. Shirzaei *et al.*, Measuring, modelling and projecting coastal land subsidence. *Nat. Rev. Earth Environ.* **2**, 40–58 (2021).
7. S.-C. Han, J. Sauber, F. Pollitz, R. Ray, Sea level rise in the Samoan Islands escalated by viscoelastic relaxation after the 2009 Samoa-Tonga earthquake. *J. Geophys. Res. Solid Earth* **124**, 4142–4156 (2019).
8. R. J. Nicholls *et al.*, A global analysis of subsidence, relative sea-level change and coastal flood exposure. *Nat. Clim. Change* **11**, 338–342 (2021).
9. L. O. Ohenhen, M. Shirzaei, C. Ojha, S. F. Sherpa, R. J. Nicholls, Disappearing cities on US coasts. *Nature* **627**, 108–115 (2024).
10. M. Govorcin, D. P. S. Bekaert, B. D. Hamlington, S. S. Sangha, W. Sweet, Variable vertical land motion and its impacts on sea level rise projections. *Sci. Adv.* **11**, eads8163 (2025).
11. P. D. Komar, J. C. Allan, P. Ruggiero, Sea level variations along the US Pacific Northwest coast: Tectonic and climate controls. *J. Coast. Res.* **27**, 808–823 (2011).
12. National Research Council et al., *Sea-Level Rise for the Coasts of California, Oregon, and Washington: Past, Present, and Future* (National Academies Press, 2012).
13. T. J. Newton *et al.*, An assessment of vertical land movement to support coastal hazards planning in Washington state. *Water* **13**, 281 (2021).
14. W. V. Sweet *et al.*, *Global and Regional Sea Level Rise Scenarios for the United States: Updated Mean Projections and Extreme Water Level Probabilities along US Coastlines* (National Oceanic and Atmospheric Administration, 2022).
15. R. J. Burgette, R. J. Weldon, D. A. Schmidt, Interseismic uplift rates for western Oregon and along-strike variation in locking on the Cascadia subduction zone. *J. Geophys. Res. Solid Earth* **114**, JB005679 (2009).
16. B. D. Hamlington *et al.*, The rate of global sea level rise doubled during the past three decades. *Commun. Earth Environ.* **5**, 601 (2024).
17. J. R. Patton *et al.*, *20th to 21st Century Relative Sea and Land Level Changes in Northern California: Tectonic Land Level Changes and Their Contribution to Sea-Level Rise* (Humboldt Bay Region, Northern California, 2023).
18. G. Garner *et al. IPCC AR6 WGI Sea Level Projections* (IPCC, 2022).
19. J. C. Allan, P. D. Komar, Extreme storms on the Pacific Northwest coast during the 1997–98 El Niño and 1998–99 La Niña. *J. Coast. Res.* **18**, 175–193 (2002).
20. J. Sepanik, "Sea level rise exposure inventory for Oregon's estuaries" (Oregon Coastal Management Program and Department of Land Conservation and Development, Salem, OR, 2017).
21. L. S. Brophy, "Modeling sea level rise impacts to Oregon's tidal wetlands: Maps and prioritization tools to help plan for habitat conservation into the future" (MidCoast Watersheds Council, Oregon Coast, Oregon, 2017).
22. M. Brand *et al.*, Impacts of a Cascadia subduction zone earthquake on water levels and wetlands of the lower Columbia River and estuary. *Geophys. Res. Lett.* **50**, e2023GL103017 (2023).
23. A. C. Kemp, N. Cahill, S. E. Engelhart, A. D. Hawkes, K. Wang, Revising estimates of spatially variable subsidence during the AD 1700 Cascadia earthquake using a Bayesian foraminiferal transfer function. *Bull. Seismol. Soc. Am.* **108**, 654–673 (2018).
24. B. F. Atwater, Evidence for great Holocene earthquakes along the outer coast of Washington State. *Science* **236**, 942–944 (1987).
25. B. F. Atwater, E. Hemphill-Haley, *Recurrence Intervals for Great Earthquakes of the Past 3,500 Years at Northeastern Willapa Bay, Washington* (USGS Professional Paper, 1997).
26. A. R. Nelson, I. Shennan, A. J. Long, Identifying coseismic subsidence in tidal-wetland stratigraphic sequences at the Cascadia subduction zone of western North America. *J. Geophys. Res. Solid Earth* **101**, 6115–6135 (1996).
27. R. C. Witter, H. M. Kelsey, E. Hemphill-Haley, Great Cascadia earthquakes and tsunamis of the past 6700 years, Coquille River estuary, southern coastal Oregon. *Geol. Soc. Am. Bull.* **115**, 1289–1306 (2003).
28. A. D. Hawkes, B. P. Horton, A. R. Nelson, C. H. Vane, Y. Sawai, Coastal subsidence in Oregon, USA, during the giant Cascadia earthquake of AD 1700. *Quat. Sci. Rev.* **30**, 364–376 (2011).
29. E. K. Peck, T. P. Guilderson, M. H. Walczak, R. A. Wheatcroft, Recovery rate of a salt marsh from the 1700 CE Cascadia Subduction Zone earthquake, Netarts Bay, Oregon. *Geophys. Res. Lett.* **49**, e2022GL099115 (2022).
30. M. A. Walton *et al.*, Toward an integrative geological and geophysical view of Cascadia subduction zone earthquakes. *Annu. Rev. Earth Planet. Sci.* **49**, 367–398 (2021).
31. K. Sieh *et al.*, Earthquake supercycles inferred from sea-level changes recorded in the corals of West Sumatra. *Science* **322**, 1674–1678 (2008).
32. M. W. Hughes *et al.*, The sinking city: Earthquakes increase flood hazard in Christchurch. New Zealand. *GSA Today* **25**, 4–10 (2015).
33. B. F. Atwater *et al.*, *Surviving a Tsunami: Lessons from Chile, Hawaii, and Japan* (US Department of the Interior, US Geological Survey, 1999).
34. W. Weischet, Further observations of geologic and geomorphic changes resulting from the catastrophic earthquake of May 1960. *Chile. Bull. Seismol. Soc. Am.* **53**, 1237–1257 (1963).
35. G. Plafker, R. Kachadoorian, E. B. Eckel, L. R. Mayo, *Effects of the Earthquake of March 27, 1964, on Various Communities* (USGS Professional Paper 542-G. U.S. Government Printing Office,1969).
36. R. S. Syamsidik Oktari, K. Munadi, S. Arief, I. Z. Fajri, Changes in coastal land use and the reasons for selecting places to live in Banda Aceh 10 years after the 2004 Indian Ocean tsunami. *Nat. Hazards* **88**, 1503–1521 (2017).
37. T. Sugano, A. Nozu, E. Kohama, K. Shimosako, Y. Kikuchi, Damage to coastal structures. *Soils Found.* **54**, 883–901 (2014).
38. K. Udo, D. Sugawara, H. Tanaka, K. Imai, A. Mano, Impact of the 2011 Tohoku earthquake and tsunami on beach morphology along the northern Sendai coast. *Coast. Eng. J.* **54**, 1250009 (2012).
39. H. Tanaka *et al.*, Coastal and estuarine morphology changes induced by the 2011 Great East Japan Earthquake Tsunami. *Coast. Eng. J.* **54**, 1250010-1-1250010–25 (2012).
40. M. D. Petersen *et al.*, The 2018 update of the US national seismic hazard model: Overview of model and implications. *Earthq. Spectra* **36**, 5–41 (2020).
41. J. von Dohlen, *Humboldt County Building & Planning Department* (GIS, Humboldt County Land Use Dataset, 2024).
42. T. Thorson *et al.*, *Land Use in Oregon in The Soils of Oregon 223–263* (Springer, 2022).
43. Washington Land Use Dataset, *Washington State Geospa8al Portal – Washington Geoservices* (Washington Land Use Dataset, 2017).
44. Washington Road Dataset, *Pacific County Department of Public Works Spatial Data* (Washington Road Dataset-, Pacific County, 2023).

45. T. Triesch, *Grays Harbor County GIS Program* (Washington Road Dataset- Grays Harbor County, 2024).
46. J. von Dohlen, *Humboldt County Building & Planning Department* (GIS, Humboldt County Road Dataset, 2024).
47. ODOT, *Oregon Department of Transportation (ODOT)* (Oregon Road Dataset, 2021).
48. Data for Good at Meta, *United States: High Resolution Population Density Maps* (Data for Good at Meta, 2020).
49. Federal Emergency Management Agency (FEMA), *USA Structures* (FEMA, 2024).
50. Microsoft Maps, *U. S. Building Footprints* (Microsoft Maps, 2018)
51. NOAA tide predictions- west coast. https://tidesandcurrents.noaa.gov/tide_predictions.html?gid=1743. Accessed 15 October 2024.
52. R. J. Tobin, C. Calfee, *The National Flood Insurance Program's Mandatory Purchase Requirement: Policies, Processes, and Stakeholders* (American Institutes for Research, 2005).
53. U. S. Geological Survey, 1/3rd arc-second Digital Elevation Models (DEMs) - USGS national map 3DEP downloadable data collection. https://www.usgs.gov/the-national-map-data-delivery. Accessed 15 October 2024.
54. D. T. Small, D. Melgar, Geodetic coupling models as constraints on stochastic earthquake ruptures: An example application to PTHA in Cascadia. *J. Geophys. Res. Solid Earth* **126**, e2020JB021149 (2021).
55. D. Melgar, Was the January 26th, 1700 Cascadia earthquake part of a rupture sequence? *J. Geophys. Res. Solid Earth* **126**, e2021JB021822 (2021).
56. P.-L. Wang *et al.*, Heterogeneous rupture in the great Cascadia earthquake of 1700 inferred from coastal subsidence estimates. *J. Geophys. Res. Solid Earth* **118**, 2460–2473 (2013).
57. L. J. Leonard, C. A. Currie, S. Mazzotti, R. D. Hyndman, Rupture area and displacement of past Cascadia great earthquakes from coastal coseismic subsidence. *GSA Bull.* **122**, 2079–2096 (2010).
58. H. Luo, K. Wang, Finding simplicity in the complexity of postseismic coastal uplift and subsidence following great subduction earthquakes. *J. Geophys. Res. Solid Earth* **127**, e2022JB024471 (2022).
59. L. Feng *et al.*, A unified GPS-based earthquake catalog for the Sumatran plate boundary between 2002 and 2013. *J. Geophys. Res. Solid Earth* **120**, 3566–3598 (2015).
60. W. J. Simons *et al.*, Vertical motion of Phuket Island (1994–2018) due to the Sumatra-Andaman mega-thrust earthquake cycle: Impact on sea-level and consequences for coral reefs. *Mar. Geol.* **414**, 92–102 (2019).
61. K. Goto *et al.*, Ten years after the 2011 Tohoku-oki earthquake and tsunami: Geological and environmental effects and implications for disaster policy changes. *Earth-Sci. Rev.* **212**, 103417 (2021).
62. Y. Hu, R. Bürgmann, N. Uchida, P. Banerjee, J. T. Freymueller, Stress-driven relaxation of heterogeneous upper mantle and time-dependent afterslip following the 2011 Tohoku earthquake. *J. Geophys. Res. Solid Earth* **121**, 385–411 (2016).
63. B. Fox-Kemper *et al.*, *Ocean, Cryosphere and Sea Level Change. in Climate Change 2021: The Physical Science Basis. Contribution of Working Group I to the Sixth Assessment Report of the Intergovernmental Panel on Climate Change, 1211–1362* (Cambridge University Press, Cambridge, United Kingdom and New York, NY, 2021), p. 2021.
64. Oregon Seismic Safety Policy Advisory Commission (OSSPAC), *The Oregon Resilience Plan: Reducing Risk and Improving Recovery for the Next Cascadia Earthquake and Tsunami*. http://www.oregon.gov/OMD/OEM/osspac/docs/Oregon_Resilience_Plan_Final.pdf (2013).
65. Q. S. Yu, J. Wilson, Y. Wang, "Overview of the Oregon resilience plan for next Cascadia earthquake and tsunami" in *10th US National Conference on Earthquake Engineering, Frontiers of Earthquake Engineering* (Earthquake Engineering Research Institute, Anchorage, AK, 2014), pp. 1–5.
66. Cascadia Rising 2016 Exercise: Cascadia subduction zone (CSZ) catastrophic earthquake and tsunami. Functional exercise: June 7–10, 2016; joint multi-state after-action report (2016).
67. L. S. Brophy, *Comparing Historical Losses of Forested, Scrub-Shrub, and Emergent Tidal Wetlands on the Oregon Coast, USA: A Paradigm Shift for Estuary Restoration and Conservation* (Institute for Applied Ecology Corvallis, OR, 2019).
68. S. Y. Teh, H. L. Koh, Climate change and soil salinization: Impact on agriculture, water and food security. *Int. J. Agric. For. Plant.* **2**, 1–9 (2016).
69. S. Mazhar, E. Pellegrini, M. Contin, C. Bravo, M. De Nobili, Impacts of salinization caused by sea level rise on the biological processes of coastal soils–a review. *Front. Environ. Sci.* **10**, 909415 (2022).
70. K. Best *et al.*, Demographics and risk of isolation due to sea level rise in the United States. *Nat. Commun.* **14**, 7904 (2023).
71. S. Yasuda, K. Harada, K. Ishikawa, Y. Kanemaru, Characteristics of liquefaction in Tokyo Bay area by the 2011 Great East Japan earthquake. *Soils Found.* **52**, 793–810 (2012).
72. K. Thorne *et al.*, US Pacific coastal wetland resilience and vulnerability to sea-level rise. *Sci. Adv.* **4**, eaao3270 (2018).
73. E. K. Peck, R. A. Wheatcroft, L. S. Brophy, Controls on sediment accretion and blue carbon burial in tidal saline wetlands: Insights from the Oregon coast, USA. *J. Geophys. Res. Biogeosci.* **125**, e2019JG005464 (2020).
74. W. E. Highfield, S. D. Brody, C. Shepard, The effects of estuarine wetlands on flood losses associated with storm surge. *Ocean Coast. Manag.* **157**, 50–55 (2018).
75. S. Temmerman *et al.*, Marshes and mangroves as nature-based coastal storm buffers. *Annu. Rev. Mar. Sci.* **15**, 95–118 (2023).
76. P. L. Barnard *et al.*, Extreme oceanographic forcing and coastal response due to the 2015–2016 El Niño. *Nat. Commun.* **8**, 14365 (2017).
77. R. C. Witter *et al.*, Simulating tsunami inundation at bandon, coos county, oregon, using hypothetical Cascadia and Alaska earthquake scenarios. *Or. Dep. Geol. Miner. Ind. Spec. Pap.* **43**, 57 (2011).
78. State of California. *Tsunami Hazard Area Map, Los Angeles County* (California Geological Survey and the California Governor's Office of Emergency Services, 2021).
79. A. Dolcimascolo *et al.*, *Tsunami Hazard Maps of the Puget Sound and Adjacent Waters–Model Results from a 2,500-year Magnitude 9.0 Cascadia Subduction Zone Earthquake Scenario. Also Available httpswww Dnr Wa Govnewsnew-Study-Details-Impacts-Tsunami-Fault-Run.--Seattle Search In* (2022).
80. T. Dura *et al.*, Changing impacts of Alaska-Aleutian subduction zone tsunamis in California under future sea-level rise. *Nat. Commun.* **12**, 7119 (2021).
81. I. Sepúlveda, P.L.-F. Liu, M. Grigoriu, J. S. Haase, P. Winckler, Non-stationary probabilistic tsunami hazard assessments compounding tides and sea level rise. *Earths Future* **10**, e2022EF002965 (2022).
82. Federal Emergency Management Agency (FEMA), *Coastal Hazards and Flood Mapping: A Visual Guide*, fema.gov/coastal-food-risk-study-process (FEMA, 2021).
83. G. G. Garner *et al.*, IPCC AR6 Sea-Level Rise Projections (2021). https://sealevel.nasa.gov/data_tools/17. Accessed 25 October 2022.
84. M. Comninou, J. Dundurs, The angular dislocation in a half space. *J. Elast.* **5**, 203–216 (1975).
85. T. Dura, DuraGEOSVT/Cascadia. GitHub. https://github.com/DuraGEOSVT/Cascadia. Deposited 11 February 2025.
86. K. Grosulak-McCord, Oregon Zoning - 2017. Oregon GeoHub. https://geohub.oregon.gov/datasets/oregon-geo::zoning/about. Accessed 15 October 2024.
87. J. von Dohlen, General Plan Land Use. Humboldt County GIS Data. https://humboldtgov.org/276/GIS-Data-Download. Accessed 15 October 2024.
88. Washington State Geospatial Portal, Washington State Land Use 2010. Washington Geoservices. https://geo.wa.gov/datasets/wa-geoservices::washington-state-land-use-2010/about. Accessed 15 October 2024.
89. Oregon Department of Transportation GIS Unit, Road Centerline Dataset. Oregon ArcGIS Hub. https://www.arcgis.com/home/item.html?id=3bc7bd2ef9e54f66886f4c095a6eb63c. Accessed 15 October 2024.
90. J. von Dohlen, Humboldt County GIS Roadway Centerline. Humboldt County GIS Data. https://humboldtgov.org/276/GIS-Data-Download. Accessed 15 October 2024.
91. Pacific County Department of Public Works, County Roads – Pacific County, WA. Pacific County GIS. https://www.co.pacific.wa.us/gis/DesktopGIS/WEB/index.html. Accessed 15 October 2024.
92. T. Triesch, Grays Harbor County Roads. Grays Harbor County GIS. https://www.graysharbor.us/departments/central_services/GISDataDownload.php. Accessed 15 October 2024.
93. Facebook Connectivity Lab and CIESIN, Columbia University, United States High Resolution Population Density Maps + Demographic Estimates. Humanitarian Data Exchange. https://data.humdata.org/dataset/united-states-high-resolution-population-density-maps-demographic-estimates. Accessed 15 October 2024.
94. Federal Emergency Management Agency (FEMA), Structure Exposure Data Layer. FEMA ArcGIS Hub. https://fema.maps.arcgis.com/home/item.html?id=0ec8512ad21e4bb987d7e848d14e7e24. Accessed 15 October 2024.
95. Microsoft, U.S. Building Footprints Dataset. GitHub. https://github.com/microsoft/USBuildingFootprints. Accessed 15 October 2024.